RESEARCH ARTICLE

Off-board aerodynamic measurements of small-UAVs in glide flight using motion tracking

M.E.M. Ouhabi [ID] and S. Narsipur [ID]

Department of Aerospace Engineering, Mississippi State University, Mississippi State, USA
Corresponding author: M.E.M. Ouhabi; Email: mo603@msstate.edu

Abstract
Measuring the aerodynamics and stability characteristics of small unmanned aerial vehicles (sUAVs) operating at Reynolds numbers below $60,000$ is a challenge. Conventional measurement methods can be impractical and costly due to the vehicle's size and the considerably low forces and moments involved. To overcome these limitations, the current study aims at utilising an existing motion tracking system to conduct off-board aerodynamic measurements of sUAVs. Six sUAVs, with varying wing aspect ratios, are investigated in un-powered, glide flight mode to establish the utility of the motion capture system as an aerodynamic characterisation system and understand the low Reynolds number effects on the flight dynamics. The trajectory tracking system was thoroughly validated through a series of static and dynamic tests to account for uncertainties and errors. Subsequently, flight trajectory data was collected and processed to extract the aircraft's force and moment characteristics under quasi-steady conditions. The measured lift, drag and moment data compared well with existing literature and theoretical predictions. Longitudinal, lateral and dynamic stability derivatives were also accurately captured. Key findings from the current work included an inverse relationship between the wing aspect ratio and lift curve slope and substantially lower Oswald efficiency factors, both of which were attributed to low Reynolds number effects.

Nomenclature

$Æ\!R$	aspect ratio
b	wingspan
$\bar{c}$	wing mean aerodynamic chord
C_D	drag coefficient
C_{D_0}	parasite drag coefficient
C_L	lift coefficient
C_{L_α}	lift curve slope
C_R	roll moment coefficient
C_M	pitch moment coefficient
C_N	yaw moment coefficient
CG	centre of gravity
D	drag force
I	inertia matrix
L	lift force
R	rotation matrix
$\bar{q}$	dynamic pressure
Re	reynolds number
S_{REF}	wing reference area
u, v, w	body fixed velocity components
V	inertial velocity

x, y, z	position components
X_{np}	neutral point
e_0	oswald efficiency factor
C_{n_β}	weather vane stability
C_{l_β}	roll stability
$\forall$	volume

Greek symbol

α	angle-of-attack
β	sideslip angle
δ_e	elevator deflection
ϕ, θ, ψ	roll, pitch and yaw angles
ω	angular velocity
$\omega_{n,ph}$	phugoid natural frequency

1.0 Introduction

The aerodynamic behaviour of small unmanned aerial vehicles (sUAVs) differ from well-established theoretical principles and empirical findings derived from full-scale aircraft [1–3], and can be primarily attributed to low Reynolds number effects. Delving into the intricacies of sUAV aerodynamics is essential for comprehending the complex interactions between the vehicle and its surrounding airflow so as to glean a thorough understanding of their performance, safety, efficiency and manoeuverability. By conducting systematic analyses, researchers and engineers can acquire valuable insights that facilitate the optimisation of design parameters and operational strategies, leading to improved overall performance and mission success. However, there remains a scarcity of aerodynamic data for sUAVs, which can be mainly attributed to the difficulties in measuring data at the low Reynolds number conditions in which sUAVs typically operate (below $60,000$) and generating the correct atmospheric conditions sUAVs are subjected to in wind tunnel testing [3, 4]. The lack of data in turn restricts our understanding and ability to develop control systems for sUAVs to efficiently manoeuver and retain control in real flight conditions. Driven by recent advancements in motion tracking technologies for the estimation of aerodynamic parameters, the objective of the current study is two-fold: (i) to verify the efficacy of motion capture systems as a dependable instrument for flight testing, thereby facilitating the comprehensive characterisation of aerodynamic and stability parameters of sUAVs, and (ii) to analyse the impact of low Reynolds number effects on the aerodynamic behaviour of sUAVs.

Currently, most of the aerodynamic data for sUAVs is obtained through wind tunnel testing. However, these methods can be costly and increase in complexity as the scale of the vehicle decreases [5–8]. Moreover, the size and weight limitations of sUAVs impose significant constraints on traditional flight testing, making it challenging to accommodate on-board flight data instrumentation [9]. Significant progress in camera technology and advanced software algorithms for data extraction have facilitated the utilisation of off-board motion tracking as an alternative approach to acquire aerodynamic data. This approach has been demonstrated to have numerous advantages over conventional wind and water tunnel testing including cost-effectiveness, simplicity and the ability to capture detailed flight data at higher frequencies across all flight conditions of sUAVs [3, 4, 10]. The method involves attaching reflective markers to the sUAV and using a set of high-frequency cameras to capture and track the markers positions and attitudes through triangulation [11]. The marker(s) captured position in a three-dimensional space with respect to time can then be used to determine the aerodynamic forces and moments acting on the sUAV [3, 4, 10–16]. Since the late 2000s, multiple researchers [4, 10, 15, 17, 18] have demonstrated the successful utilisation of in-flight trajectory sampling for extracting aerodynamic characteristics for fixed-wing micro air vehicles (MAVs). Extensive research utilising motion capture trajectory sampling was carried out by Uhlig et al. [3, 11, 14, 19] to comprehensively investigate a wide range of flight

regimes on various sUAVs with wing aspect ratios ranging from 2.5 to 12. Parallel research by Rao et al. [12] effectively employed a motion capture system to implement a thrust model for powered flight, yielding successful outcomes. Furthermore, Cory et al. [17, 18], Paranjape et al. [20] and Moore [21] successfully utilised motion capture systems for control modeling, showcasing their efficacy in capturing and analysing motion dynamics and highlighting the valuable role of motion capture systems in advancing control modeling techniques.

One of the notable observations regarding sUAV aerodynamics made by Uhlig et al. [11, 19] is the deviation of experimental forces and moments measurements from theoretical predictions and large-scale aircraft flight data for all sUAVs investigated in their studies. These deviations are primarily attributed to scaling and low Reynolds number effects, and are in line with deductions made by other researchers regarding low Reynolds number sUAV flight operations [1, 2]. Therefore, attaining an in-depth understanding of low Reynolds number effects on sUAV flight dynamics is necessary to effectively advance the technology. While restrictive for full-configuration sUAVs, the existing body of experimental research provides a good understanding of the effects of low Reynolds number flows on aerofoil and wing aerodynamics [5–7, 22–28]. Particular to wing aerodynamics in low Reynolds number flows, Spedding and McArthur [23] conducted an exhaustive study on flow behaviour at said conditions and described the concept of a down-scaling factor to refine the prediction of aerodynamic characteristics for $Re < 100,000$. Subsequent research by Ananda et al. [27, 29], aimed at establishing a correlation between low Reynolds number effects and aspect ratio, showed a consistent decrease in the Oswald efficiency factor with increasing wing aspect ratio.

Building upon the existing state-of-the-art depicted in the literature, the present study seeks to establish the off-board capability of estimating aerodynamic parameters for sUAVs during glide flight for an existing motion-capture system. A comprehensive analysis is subsequently conducted on the aerodynamics of various full-scale sUAVs with wing aspect ratios ranging between 2.56 and 6.32, with the aim of understanding the effects of low Reynolds number flows on sUAV aerodynamics and stability. The current work will serve as the first step to the future development of off-board aerodynamic estimation capabilities of sUAVs in powered level- and manoeuvering-flights in flow conditions typically encountered during real flight. The following section (Section 2) details the experimental data acquisition system. In Section 3, the data collection and processing techniques are discussed in detail. System uncertainity, flight repeatability tests and data filtering methods used in the current work are detailed in Section 4. Following this, the flight results for the baseline aircraft are analysed and compared against theory and existing literature in Section 5. Finally, Section 6 summarises the conclusions drawn from the results and provides future research directions.

2.0 Experimental apparatus

2.1 Motion capture system

Experiments were conducted in the Autonomous Systems Research Laboratory (ASRL) located at the Raspet Flight Research Laboratory. The ASRL is equipped with an OptiTrack [30] system that is composed of a set of 12 *Prime*^{x}41 cameras placed at a height of 5.4864m, and covering a test area of 14.516m × 9.611m (Fig. 1). The cameras have a resolution of 4.1 megapixels and frame rates reaching 250Hz, and are equipped with a low distortion lenses called fast glass. The 12mm lens is treated with anti-reflective coating. Additionally, the cameras have a 10 bit grayscale depth leading to lower noise and highly improved precision. Data provided by the developers state that positional errors are less than ±0.10mm and rotational error are smaller 0.5 degrees for a reference (9m × 9m) tracking area. The system features integrated image processing allowing for precise marker centre detection. To triangulate an object, reflective markers (that come in different shapes and sizes) are placed on the object's surface. The Motive Optical motion capture software is used to gather the motion capture data.
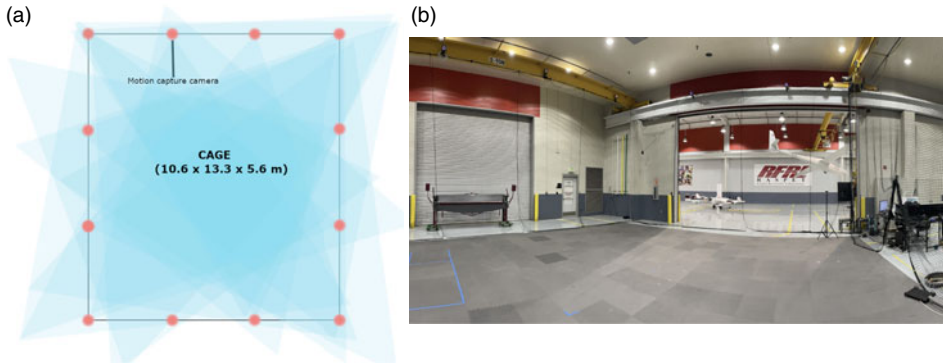
Figure 1. *Optitrack system: (a) camera placement and field of view and (b) test area.*

Prior to using the OptiTrack system, a calibration routine is carried out to get the best possible results and keep the residual values to a minimum. Several calibration methods were studied in order to get a consistent residual throughout testing. The final method used for calibration is the wanding technique where a wand containing three spherical marker is moved in the capture volume, after the control volume is prepared and optimised for calibration by masking any extraneous reflections and unnecessary markers. The wanding technique involves collecting a sufficient number of samples by waving the wand gently across the entire capture volume. For the current work, a calibration threshold was reached when each camera captured 12,000 points covering the majority of the capture volume. This translated to a residual range of 0.4–0.55mm which was considered exceptional by the software's algorithm. Consistent residual is of high importance through testing, and for small dynamic testing times typically ranging from 1 to 2 seconds, very small variations were observed.

2.2 Rail system

A 1.2m linear rail launch system was designed to launch the aircraft. As shown in Fig. 2, the system is mounted on an adjustable angle bracket that allows launching slope angles ranging from 0 to 90 degrees. A release mechanism composed of an electromagnet, a stepper motor and an ultrasonic sensor was implemented to release the aircraft once a predefined travel distance threshold was reached.

2.3 Aircraft

A set of six aircraft, shown in Fig. 3, were used in the current study to validate the efficacy of the motion capture system in characterising sUAV flight dynamics and studying low Reynolds number effects on the aerodynamics. Square reflective markers were placed on the aircraft surface to allow the motion capture system triangulate the sUAV. The markers were placed in a manner that allowed for the least amount of standard deviation in the captured data. The only modifications to the out-of-the-box aircraft was the removal of the battery and the replacement of the propeller with a 3D-spherical marker to enhance aircraft's detectability within the testing environment. As it was crucial to accurately establish the geometric constants of the sUAVs to ensure precise analysis and evaluation of their aerodynamic behaviour, geometric property estimation was carried out by digitising the surfaces of interest. Wing surface areas were determined using Green's theorem. To determine the inertial moments of the aircraft, the pendulum swing measurement technique [31] was employed. Table 1 provides mass and geometric details for all six sUAVs used in the current study.
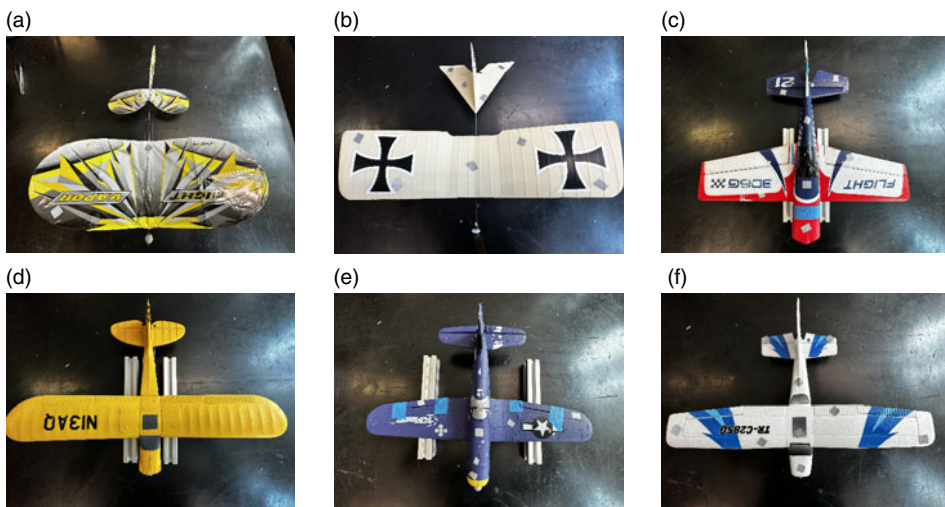
Figure 2. *Linear rail system with hinged F4U-Corsair.*

Figure 3. *(a) UMX-Vapor (b) Micro Vintage Stick (c) Edge A-430 (d) S2-CUB (e) F4U-Corsair (f) TR-C285G.*

3.0 Data collection and processing

The Optitrack system creates a rigid frame by triangulating the earth-referenced position of markers placed on the aircraft and returns the positional ($[x_e \; y_e \; z_e]$) and Euler angles ($\phi \; \theta \; \psi$) data in the earth-referenced axis system. The data collected has to be filtered to account for noise. Based on multiple smoothing methods that were investigated by Uhlig [3], a third order linear regression filter implementing the Savitzky-Golay algorithm was used for position and attitude smoothing, as shown in Fig. 4. The R^2 values observed for the third-order Savitzky-Golay filter applied to the raw data for each flight were above 0.985 for all measured variables. In this instance, R^2 values of 0.999, 0.997, 0.996 were obtained for roll, yaw, and pitch fitted data, respectively.

Table 1. *Aircraft properties*

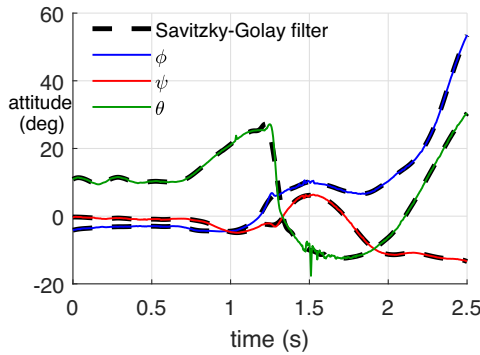|	UMX-Vapor	MVS	A-430	S2-CUB	F4U-Corsair	TR-C285G
Mass (g)	23	22.7	63.5	35	47.7	31.4
Span (cm)	37.6	44	43	40	40	40
S_{ref} (cm^2)	552.25	505.5	409	253.1	281.69	264.88
$\mathcal{R}$	2.56	3.8	4.5	6.32	5.68	6.05
Length (cm)	41.9	35.5	40	28.5	29	31
I_{xx} (g.cm^2)	374	423	1,074	686	723	721
I_{yy} (g.m^2)	926	1,286	1,774	1,423	934	2,614
I_z (g.cm^2)	1,179	1,460	4,661	3,084	2,043	3,307
I_{xz} (g.cm^2)	82	28	140	65	20	77

Figure 4. *Filter application on attitude data for the UMX-Vapor.*

To transform the earth-referenced frame to the body-referenced frame (aligned such that the nose is along the positive *x*-axis and the right wing is along the positive *y*-axis), a rotation matrix is used [3, 4, 11, 14, 19].

$$R = \begin{bmatrix} \cos(\theta)\cos(\psi) & \cos(\theta)\cos(\psi) & -\sin(\theta) \\ -\cos(\phi)\sin(\psi) + \sin(\phi)\sin(\theta)\cos(\psi) & \cos(\phi)\cos(\psi) + \sin(\phi)\sin(\theta)\sin(\psi) & \sin(\phi)\cos(\theta) \\ \sin(\phi)\sin(\psi) + \cos(\phi)\sin(\theta)\cos(\psi) & -\sin(\phi)\cos(\psi) + \cos(\phi)\sin(\theta)\sin(\psi) & \cos(\phi)\cos(\theta) \end{bmatrix} \tag{1}$$

An off-set matrix and off-set vector are computed to translate the system captured centre of gravity (henceforth referred to as the centroid) to the actual aircraft CG. The Euler angles are then extracted from the new rotation matrix, R_{EB}, given as,

$$R_{EB} = R_{ET} R_{TB} \tag{2}$$

where R_{ET} is the rotation from earth to centroid frame of reference and R_{TB} is the rotation from centroid to body/CG frame of reference. Angular velocity, angular acceleration, translational velocity and translational acceleration in the body frame are computed in a manner similar to that employed in Refs (3, 4). The body acceleration is then calculated using the equation,

$$a_b = R_{EB}[\ddot{x}_e \ \ddot{y}_e \ \ddot{z}_e]^T + \dot{\omega} \times \vec{r} + \omega \times (\omega \times \vec{r}) \tag{3}$$

where $\vec{r}$ is the translation vector from the rigid body centroid to the UAV centre of gravity and ω is the angular acceleration, whose components (p, q, r) are calculated as,

$$\begin{bmatrix} p \\ q \\ r \end{bmatrix} = \begin{bmatrix} 1 & 0 & -\sin(\theta) \\ 0 & \cos(\phi) & \sin(\phi)\cos(\theta) \\ 0 & -\sin(\phi) & \cos(\phi)\cos(\theta) \end{bmatrix} \begin{bmatrix} \dot{\phi} \\ \dot{\theta} \\ \dot{\psi} \end{bmatrix} \tag{4}$$

The body velocity components (u, v, w) of the UAV are determined using equation,

$$[u \ v \ w]^T = R_{EB}[\dot{x}_e \ \dot{y}_e \ \dot{z}_e]^T + (\omega \times r) \tag{5}$$

Subsequently, the total velocity, angle-of-attack, and sideslip angle are using equations,

$$V = \sqrt{u^2 + v^2 + w^2} \tag{6}$$

$$\alpha = \tan^{-1}(w/u) \tag{7}$$

$$\beta = \sin^{-1}(v/V) \tag{8}$$

The aerodynamic forces and moments acting on the body are then calculated as,

$$F_{aero} = F_{ext} - F_G \tag{9a}$$

$$F_{ext} = ma_b \tag{9b}$$

$$F_G = mg[-\sin(\theta)\sin(\phi)\cos(\theta)\cos(\phi)\cos(\theta)]^T \tag{9c}$$

$$L = -F_{aero,z}\cos(\alpha) + F_{aero,x}\sin(\alpha) \tag{10}$$

$$D = -F_{aero,z}\sin(\alpha)\cos(\beta) + F_{aero,x}\cos(\alpha)\cos(\beta) - F_{aero,y}\sin(\beta) \tag{11}$$

$$M_{ext} = I\dot{\omega} + \omega \times I\omega \tag{12}$$

Subsequently, the aerodynamic forces and moment coefficients and evaluated as,

$$C_L = \frac{L}{\bar{q}S_{REF}} \tag{13}$$

$$C_D = \frac{D}{\bar{q}S_{REF}} \tag{14}$$

$$C_M = \frac{M_{ext_y}}{\bar{q}S_{REF}\bar{c}} \tag{15}$$

4.0 Uncertainty analysis, flight repeatability, and data filtering

4.1 Uncertainty analysis

The uncertainty analysis of the motion capture system was done through a set of static and dynamic tests, detailed in the following subsections.

4.1.1 Static tests

The standard deviation in position and attitude measured by the motion capture system was investigated using the F4U-Corsair and UMX Vapor aircraft. Table 2 shows the standard deviation in positional and angular data at measurement frequencies ranging from 200 to 250Hz. It was observed that measuring at a higher frequency resulted in higher standard deviations. While the deviation in measured values

Table 2. *Standard deviations in position and attitude with respect to frequency*

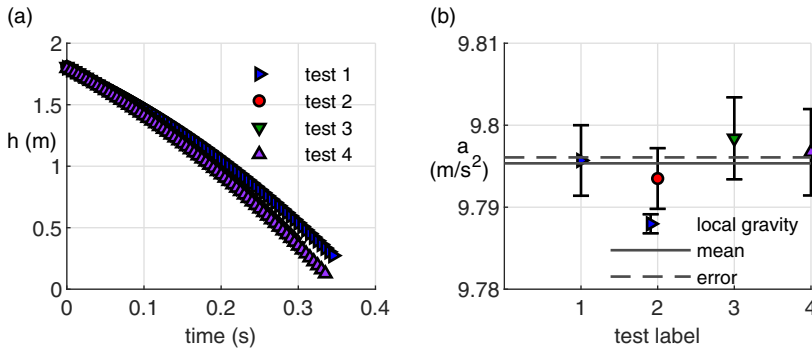| Aircraft	Frequency	Position (mm)			Attiude (deg)			Wingspan (cm)
		σ_x	σ_y	σ_z	σ_ϕ	σ_θ	σ_ψ	
F4U - Corsair	200Hz	0.05733	0.03842	0.02377	0.01035	0.00942	0.01225	40.0
	225Hz	0.09361	0.06553	0.03467	0.04168	0.01353	0.01202	
	250Hz	0.08307	0.0504	0.03393	0.02013	0.01303	0.01166	
UMX Vapor	200Hz	0.05502	0.05648	0.03184	0.02315	0.00784	0.03644	37.6

Figure 5. *Free-fall tests: (a) height versus time for different drop tests (b) mean acceleration due to gravity and resulting error.*

could be attributed to vibrations occurring along a particular axis, they were still comparable to, and at most times lesser than the standard deviations of the motion-capture systems used by other researchers [3, 4]. Based on the current results and literature [3], a measuring frequency of 200Hz was used for the study.

4.1.2 Dynamic tests

To demonstrate the accuracy of the motion capture system in measuring acceleration, the acceleration due to gravity of an object under free-fall conditions was measured. A 5.4kg shot-put ball with a smooth finish was equipped with nine reflective sticker markers and released from an initial height of 2.8m. However, data was only analysed between a height of 1.8 and 0.1m to remove the effects of release and impact (Fig. 5(a)). The mean acceleration due to gravity for four runs was measured to be 9.7978m/s^2, as seen in Fig. 5(b). On comparing the result to the local gravity value of 9.79535m/s^2 (at Raspet II Laboratory, Starkville, MS) [32], we observed that the prediction error in acceleration by the system was 0.025%, which is within the acceptable error range.

To explore uncertainties in angular rotation, additional testing was conducted using a US-digital optical encoder connected to a dual shaft step-motor and a rotating bar. The motion capture system tracked the movement, measuring an error smaller than 0.28 degrees for a (14.5m × 9.6m) capture volume.

4.1.3 Uncertainty propagation

The root sum square (RSS) method was implemented to measure the uncertainty propagation from the Optitrack outputs $(x, y, z, \phi, \theta, \psi)$ to the aerodynamic parameters [33]. The standard deviation obtained is Section 4.1.1 are combined as shown in Equation (18), where M denotes a general measurement function such that $M = f(x, y, z, \phi, \theta, \psi)$ referring to an aerodynamic parameter $(\alpha, \beta, \ldots)$.

Table 3. *Aerodynamic parameter uncertainties*

Aircraft	V (m/s)	α (deg)	β (deg)	C_L	C_D	C_M
UMX-Vapor	0.0032	0.0024	0.0053	0.0108	0.008	0.0004
F4U-Corsair	0.0013	0.0012	0.0023	0.0156	0.014	0.0007
A-430	0.0011	0.0012	0.0011	0.0143	0.0134	0.0008
MVS	0.0014	0.0015	0.0021	0.015	0.0147	0.0009
S2-CUB	0.0004	0.0011	0.0003	0.002	0.0032	0.0002
TR-C285G	0.0024	0.0025	0.0027	0.0211	0.0026	0.001
Mean	0.0016	0.00165	0.0023	0.0131	0.0093	0.00066

$$\sigma_{combined} = \sqrt{\left(\frac{\partial M}{\partial x}\sigma_x\right)^2 + \left(\frac{\partial M}{\partial y}\sigma_z\right)^2 + \left(\frac{\partial M}{\partial z}\sigma_z\right)^2 + \left(\frac{\partial M}{\partial \theta}\sigma_\theta\right)^2 + \left(\frac{\partial M}{\partial \phi}\sigma_\phi\right)^2 + \left(\frac{\partial M}{\partial \psi}\sigma_\psi\right)^2} \quad (16)$$

The partial derivatives of the aerodynamic parameters listed in Section 3 were found and the respective propagated uncertainties are listed in Table 3.

4.2 Flight repeatability

To deduce the consistency of the flight path obtained using the rail-launch system described in Section 2.2, the UMX Vapor aircraft was launched using the rail system at a set trim angle. Figures 6(a)–(c) shows the recorded positions for four flights of the UXM Vapor. The tests showed variation along the y-axis, but little to no variance along the x and z axes. Drift along the y-axis was attributed to the way the aircraft was hinged on the rail system. The lift and drag coefficients in glide flight were estimated by processing the position and attitude data, and truncating the time history to the area of interest of the flight (Fig. 6(d)–(e)). For the UMX Vapor in glide, C_L ranged from 0.25 to approximately 0.3 and C_D fluctuated around a value of 0.1 in glide flight. While not plotted, similar fluctuations were observed for the other sUAVs as well. As the limits of the deviations in force coefficients during glide flight seen in the current tests were comparable to those observed by Uhlig [3], it was concluded that the rail system provided consistent launch characteristics. However, due to difficulties with resetting the rail system after every launch, hand-launched flight data was also used in combination to allow for a larger amount of data to be collected and analysed.

4.3 Quasi-steady data filtering

Achieving perfect glide flight (and therefore steady flight) for every launch (via the rail-system or hand-launch) can be a very time consuming and cumbersome process. Therefore, quasi-steady flight data was considered to study glide flight to enable larger data sets for analysis. Figure 7(a) shows the drag polars obtained for 24 flights of the UMX Vapor at different elevator deflections (in black), and therefore different trim angles. When considering the full flight trajectories, coefficients of lift and drag were observed to go as high as 2.5 and 2 respectively due to unsteady effects and aggressive stalls. In an effort to filter the data such that the unsteady effects are negligible, low angular rate (LAR) conditions were applied to the cumulative dataset. Based on the available literature [3, 12, 13], the conditions needed for LAR were $\dot{\alpha} < 20\mathrm{deg/s}$ and $\dot{\beta}, p, q, r < 30\mathrm{deg/s}$. Additionally, the sampled data was restricted to lift coefficients values below stall. On applying the data filter based on LAR and C_L limits to the UMX Vapor data shown in Fig. 7(a), quasi-steady flight data was obtained (red markers). On evaluating the reduced frequency (k) for the quasi-steady data, we see that the filtered data was within (k) limits of ± 0.03. As quasi-steady flight can be considered as long as $|k| < 0.05$ [14, 34], the above data
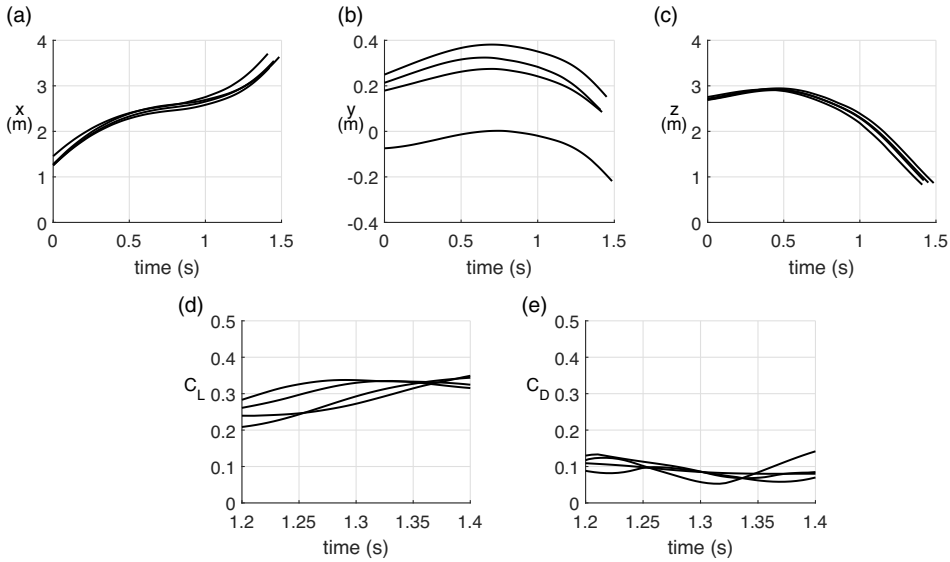
Figure 6. *Flight repeatability tests for the UMX Vapor. Variation in (a) x, (b)y, (c) z, (d) C_L and (e) C_D with time.*
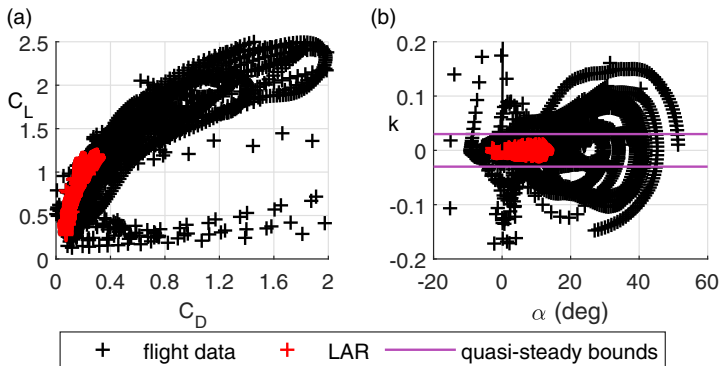

Figure 7. *(a) Full lift and drag data co-plotted with sampled LAR data (b) reduced frequency as a function of α.*

filtering scheme has been used for the remainder of the analysis to study glide-flight aerodynamics of the sUAVs.

Figure 8 plots the experimentally measured lift coefficient, C_L, for the entire sUAV alongside the augmented lift coefficient due to unsteady effects, represented by $\Delta C_{L,k} = C_{L_\alpha} k \left(\frac{1}{2} - a \right)$, where a was assumed to be -0.5 at the quarter chord. Observations show that the constraints on the angular rates eliminated unsteady flights and any possible uncertainties in the data due to un-modelled unsteady effects. The scatter observed in the data is expected and can be attributed to, but not solely limited to, time lag effects and laminar separation bubbles. However, despite this variability, linear stability derivatives such as C_{L_α} exhibited consistent trends due to their inherent robustness, similar to observations made by Rinehart and Mettler [10]. These trends are further discussed in the following section.
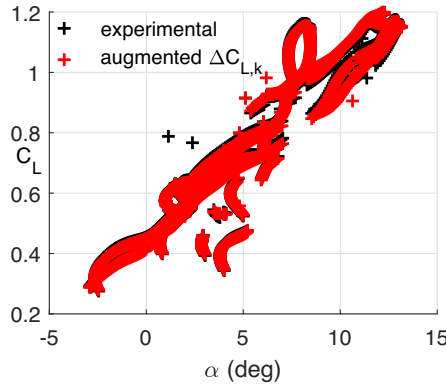
Figure 8. *Comparison between experimentally measured C_L and augmented C_L due to unsteady effects.*

5.0 Results and discussion

5.1 Flight data

The current section presents the flight data for the sUAVs tested. For the sake of brevity, detailed discussion is presented for three sUAVs: the F4U-Corsair, TR-C285G and UXM Vapor, as these were observed to best represent the corner cases. Flight data for the remainder three sUAVs have been presented in the Appendix.

5.1.1 F4U-Corsair

Flight data for the F4U-Corsair ($AR = 5.68$) sUAV was collected over 192 flights, with each flight generating approximately 200 data points. Velocity data showed that the wing chord-based Reynolds number varied between 15,000–40,000. On applying the LAR and C_L limit conditions, quasi-steady (a) drag polar, (b) lift curve, (c) drag curve and (d) pitching moment were measured and have been plotted in Fig. 9. The Oswald efficiency factor (e_o) for the F4U-Corsair was calculated to be 0.31 based on the the parabolic fit $C_D = 0.073 + 0.18C_L^2$ (co-plotted in Fig. 9(a)). This e_0 value, while much lower than that for conventional aircraft (typically $0.7 - 0.85$), was comparable in magnitude to measurements made by Spedding and McArthur [23], who observed an e_o of 0.53 for an aspect ratio 6 wing with an Eppler 387 aerofoil section operating in a $Re = 20,000$ flow. Spedding and McArthur [23] attributed the reduced values of e_o to low Reynolds number effects.

First order linear regression was applied to the C_L vs. α data to obtain the lift curve for the full aircraft (Fig. 9(b)). Additionally, the lift curves for the wing and tail surfaces were isolated by using equations,

$$C_{L_w} = \frac{C_{M_{cg}} - C_{M_{ac,w}} + C_L \left(\bar{x}_{ac,h} - \bar{x}_{cg} \right)}{\left(\bar{x}_{ac,h} - \bar{x}_{ac,w} \right)} \tag{17a}$$

$$C_{L_h} = \frac{C_{M_{ac,w}} - C_{M_{cg}} + C_L \left(\bar{x}_{cg} - \bar{x}_{ac,w} \right)}{\frac{S_h}{S_{ref}} \eta_h \left(\bar{x}_{ac,h} - \bar{x}_{ac,w} \right)} \tag{17b}$$

and have been co-plotted in Fig. 9(b). While C_L and $C_{M_{cg}}$ were calculated using the position and attitude measurements from the motion capture system, the pitching moment coefficient, $C_{M_{ac,w}}$, for the isolated wing was determined to be -0.17 using XFLR5. The values of $C_{M_{ac,w}}$ were observed to vary between -0.04 and -0.3 throughout the Reynolds number flight envelope of the F4U-Corsair over an angle-of-attack range from -5 degrees to 20 degrees. The dynamic pressure ratio (η_h) was assumed to be 0.9, based on Ref. (3). The aerodynamic chord of the wing and horizontal tail ($\bar{x}_{ac,w}, \bar{x}_{ac,h}$) were approximated to be
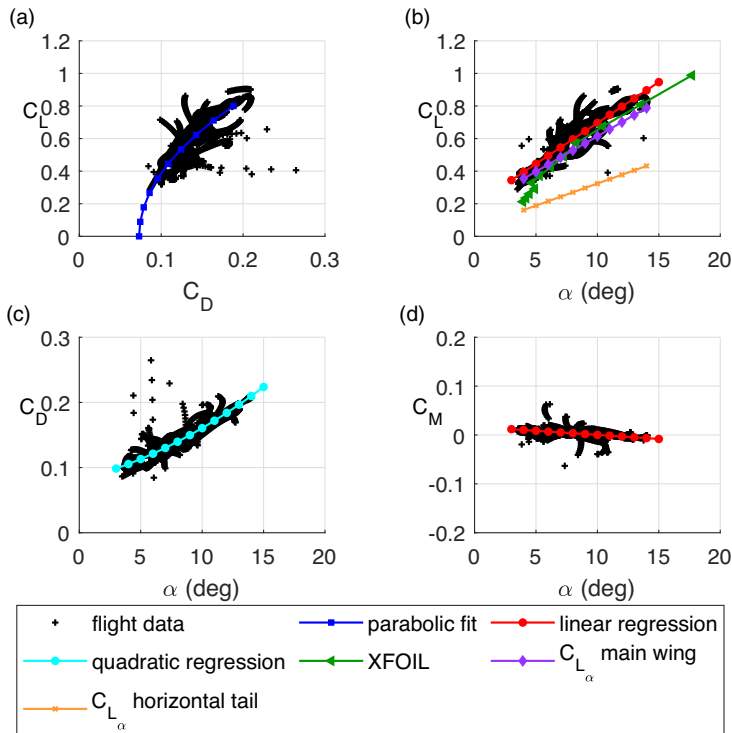
Figure 9. *Flight data for the F4U-Corsair ($\mathcal{R} = 5.68$): (a) experimental drag polar with parabolic fit, (b) experimental lift curve with linear regression, (c) experimental drag curve with quadratic regression and (d) experimental pitching moment with linear regression.*

25% and the CG location was measured using a point balance. The lift curve slopes for the full aircraft as well as the isolated wing were determined to be 2.88 and 2.38/rad, respectively. Lifting-line theory, on the other hand, predicted a lift-slope of 4.64/rad. This significant over prediction ($\sim 51.28\%$ with respect to the isolated wing) in the lift curve slope by theory was not only attributed to low-*Re* effects but also the fact that the F4U-Corsair's wing loading cannot be approximated by an ideal elliptical distribution due to its taper and dihedral. Furthermore, investigations by Uhlig [3] showed that, for a similar sUAV of equal wingspan and slightly lower $\mathcal{R}$ of 5.12 in glide flight, a 27.27% over-prediction by theory was reported when compared to measurements, for an operating Reynolds number of $\sim 26,000$.

In an attempt to further validate the measurements, the experimental C_L vs. α data was compared with viscous results from XFOIL using the aerofoil section of the F4U-Corsair. The assumptions made for this analysis were (i) all the lift is being generated by the wing and (ii) the wing is assumed to be rectangular with no taper or dihedral. The sectional wing coordinates were physically extracted from two different sections along the wing span – wing root (S1) and 75% span (S2), as shown in Fig. 10(a). Upon non-dimensionalising the coordinates, we concluded that the same aerofoil section was used for the entire wing section (Fig. 10(b)). A final, clean aerofoil profile was generated using the extracted sectional coordinates and analysed in XFOIL for a *Re* range of $15,000 - 40,000$. The full aircraft C_L versus α was then calculated by determining the glide angle-of-attack at the $Re\sqrt{C_L}$ value for the F4U-Corsair in glide (Fig. 10(c)), which equated to a value of 1.8×10^4. The glide C_L was then determined from XFOIL data for the corresponding $Re - \alpha_{glide}$ combination. When co-plotted with the experimental results (Fig. 9(b)), we see that the first-order fit for the isolated wing obtained from the flight data compares well for angles of attack above 5 degrees. The mismatch at lower angles of attack can be attributed to the lack of sufficient flight data at said conditions. Overall, the XFOIL analysis helped ascertain that the lift measurements
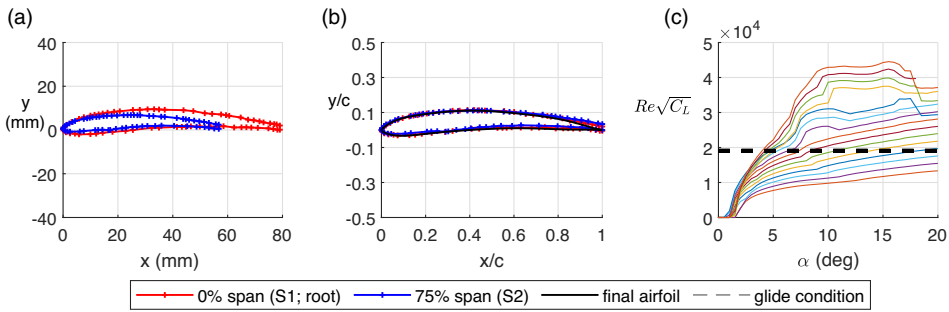
Figure 10. *Wing sectional coordinates and XFOIL analysis: (a) extracted coordinates, (b) aerofoil generated for analysis and (c) $Re\sqrt{C_L}$ for the operating Reynolds number range.*

made by the motion capture system as well as the trends predicted were logical and in line with what should be expected.

Second-order quadratic and first-order linear regressions were applied to the drag (Fig. 9(c)) and the pitching-moment (Fig. 9(d)) data, respectively. Both metrics showed similar trends when compared to flight data for a comparable aircraft (SU-26XP, $Æ= 5.12$) investigated by Uhlig [3].

5.1.2 TR-C285G

To gain deeper insights into the impact of low Reynolds numbers and confirm the patterns observed for the F4U-Corsair (Section 5.1.1), the TR-C285G model was selected for analysis. This particular model features a simplified wing design, closely resembling a rectangular wing with no dihedral effects and a moderate taper ratio. Additionally, the TR-C285G has an aspect ratio of 6.05, which closely aligns with the aspect ratio of the F4U-Corsair ($Æ = 5.68$). Flight data was obtained across 70 flights and 14 trim angles. Velocity data showed the wing chord-based Reynolds number varying between 20,000–40,000. Figure 11 plots the (a) drag polar, (b) lift curve, (c) drag curve, and (d) pitching moment for the TR-C285G aircraft. Additionally, Fig. 11(a) plots the drag polar obtained for a second set of flight tests conducted independently of the initial flight tests in order to examine measurement repeatability. The resulting parabolic fits for both flight data sets were $C_D = 0.08 + 0.17C_L^2$ and and $C_{D_2} = 0.083 + 0.172C_L^2$, respectively. The attendant Oswald efficiency factors for the two data sets were calculated to be 0.309 and 0.305, respectively, thereby showing that the motion capture system was capturing flight data across the full operating regime in a repeatable manner. The slight reduction in e_o for the TR-C285G aircraft when compared to the F4-U Corsair's 0.31 can be attributed to the marginally higher $Æ$. This deduction was confirmed by conclusions made by Ananda et al. [27] who, while conducting experiments on wings with different aspect ratios, observed a reduction in the Oswald efficiency factor with increasing $Æ$ at low Reynolds numbers. Analysis of the experimental lift curve of the TR-C285G also showed similar trends to those observed for the F4U-Corsair, with the slope from the first order regression of the isolated wing equating to 2.2/rad (compared to 2.38/rad for the F4U-Corsair). Additionally, similar to the F4U-Corsair, the lift curve slope was measured to be $\sim 46.61\%$ lower than that predicted by lifting-line theory ($C_{L\alpha}$, lifting-line = 4.72/rad), and could once again be attributed to low-*Re* effects. Overall, trends in the aerodynamic flight data for the TR-C285G matched well with that of the F4U-Corsair, thereby giving further credence to the ability of the motion capture system to effectively measure sUAV aerodynamics.

5.1.3 UMX Vapor

To test the quality of flight data measured and the low-*Re* effects for low- $Æ$ aircraft, the aerodynamic performance for the UMX Vapor ($Æ = 2.56$) was investigated. Data across a total of 24 flights at
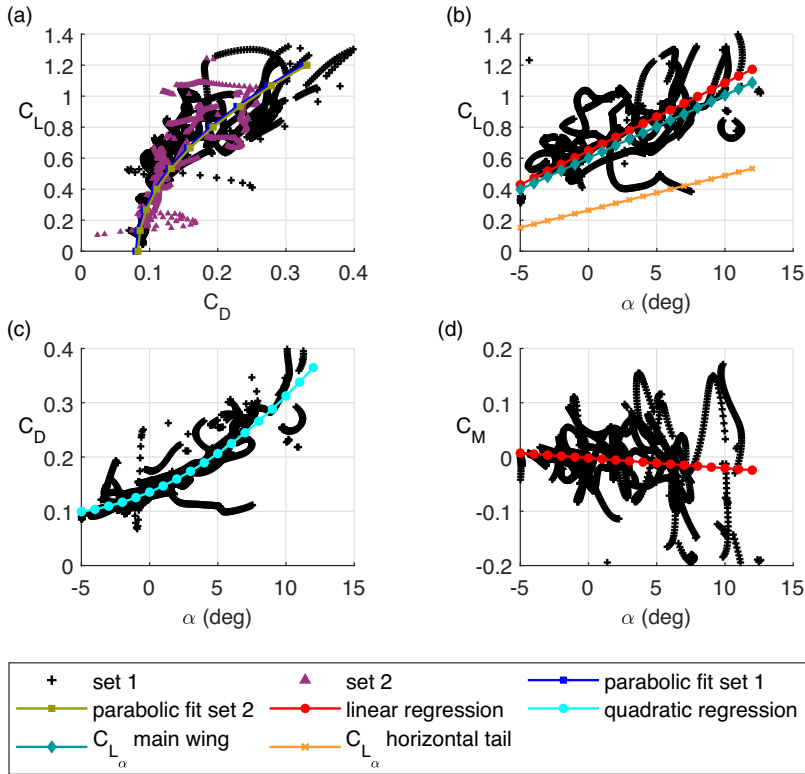
Figure 11. *Flight data for the TR-C285G (Æ= 6.05): (a) experimental drag polar with parabolic fit, (b) experimental lift curve with linear regression, (c) experimental drag curve with quadratic regression and (d) experimental pitching moment with linear regression.*

different trim angles/elevator deflections was processed and filtered to obtain the force and moment coefficient characteristics of the UMX Vapor. Figure 12 shows the experimentally computed (a) drag polar, (b) lift curve, (c) drag curve and (d) pitching moment for the UMX Vapor based on the sampled LAR and the corresponding first/second order least square regression fits. An additional, independently measured flight data set was also analysed to ascertain measurement repeatability.

The parabolic fits computed for the drag polars of the two flight data sets (Fig. 12(a)) yielded Oswald efficiency factors of 0.71 and 0.72, respectively. While much higher than the values obtained for the higher $Æ$ sUAVs (0.3113 for the F4U-Corsair and 0.307 for the TR-C285G aircraft), the magnitude of the measured e_o for the UMX Vapor are in line with observations made by Ananda et al. [27], who reported an Oswald efficiency factor of ~ 0.81 for an $Æ = 2$ flat-plate wings at low Reynolds numbers ($60,000 \leq Re \leq 200,000$). Calculation of the lift curve slope from the first-order regression curve yielded a value of 3.29/rad, which compared very well with the lifting-line theory prediction of 3.53/rad. This is in contrast to the observations made for the F4U-Corsair and TR-C285G aircraft, and could be attributed to the UMX Vapor's flat-plate, elliptically loaded wing. A detailed analysis on the trends observed and the contrasting results between the sUAVs tested is presented in the following section (Section 5.2). However, it should be noted that the overall trends in the aerodynamic data obtained for the UMX Vapor are in close agreement with results obtained by Uhlig [3] for the exact aircraft with the only difference being in the wing camber (symmetric wing in the current study versus a cambered wing in Ref. (3)). Consequently, a difference of 32.39% and 36.39% in e_o and $C_{L\alpha}$ were observed between the current measurements and Ref. (3).
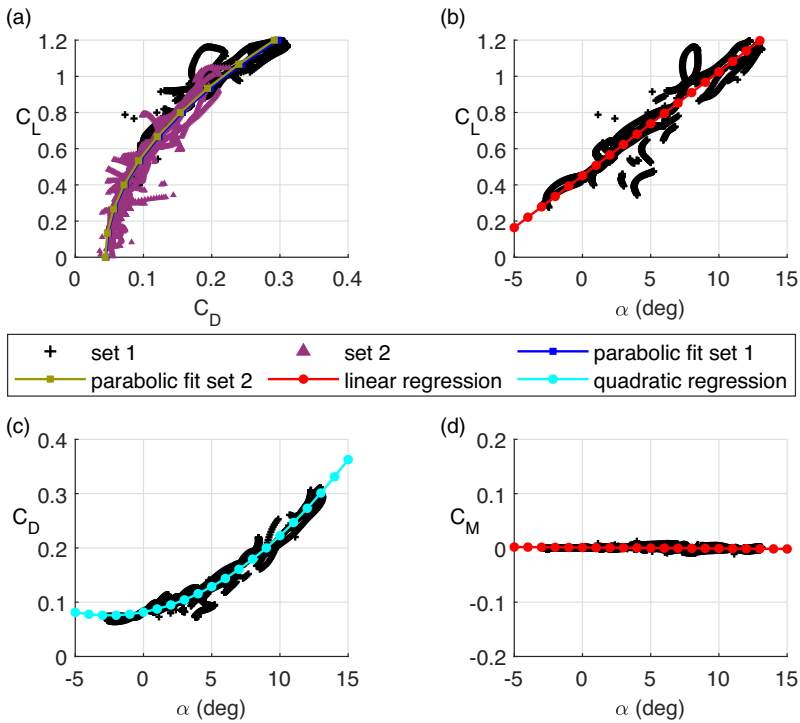
Figure 12. *Flight data for the UXM Vapor ($Æ = 2.56$): (a) experimental drag polar with parabolic fit, (b) experimental lift curve with linear regression, (c) experimental drag curve with quadratic regression and (d) experimental pitching moment with linear regression.*
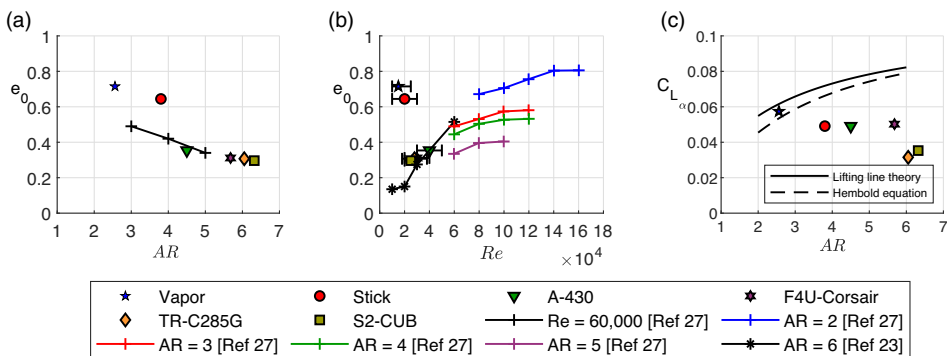

Figure 13. *(a) Oswald efficiency e_0 factor with respect to aspect ratio $Æ$ compared to literature, (b) Oswald efficiency e_0 factor with respect Reynolds number Re compared to literature (c) Lift curve slope C_{L_α} with respect to aspect ratio $Æ$ compared to theory.*

5.2 Efficiency analysis

To gain deeper insights into the effects of low Reynolds numbers on sUAV aerodynamics, trends in Oswald efficiency factors and lift-curve slopes with aspect ratio and Reynolds number for all six aircraft ($2.56 \leq Æ \leq 6.30$) are plotted (in Fig. 13) and analysed.

Figure 13(a) plots the Oswald efficiency factor (e_0) obtained from the drag polar for each sUAV with respect to $Æ$ and compares it with results obtained by Ananda et al. [27] for flat-plate wings. It is noted

that the reference data has been obtained at $Re = 60,000$ while the Reynolds number range for the aircraft tested is lower and varies between $10,000$ to $50,000$. However, both data sets are firmly in the low-Re regime, therefore allowing us to verify the current measured trends and make appropriate deductions. Results obtained from the six sUAVs show that increasing the aspect ratio leads to a decrease in e_0, therefore adhering to the trends observed by Ananda et al. [27]. However, while the magnitude of e_0 for the sUAVs with $Æ > 4$ align with those measured by Ananda et al. [27], it is over predicted for $Æ < 4$. This could be attributed to the much lower operating Reynolds number range of the Vapor and Stick aircraft ($10,000 < Re < 25,000$). Next, we compare the variation of e_0 with Re against experimental results for flat plates with $Æ$ ranging from 2 to 5 [27] and an Eppler 387 wing with $Æ = 6$ [23] in Fig. 13(b). Observations show that the e_0 measured for all aircraft with $Æ > 4$ and operating at $Re > 20,000$ matches well with Spedding and McArthur [23]. However, a sharp increase in e_0 is observed for the Vapor and Stick aircraft ($Æ < 4$). Based on the above behaviour, it can be concluded that, while, in general, an increase in $Æ$ leads to a decrease in e_0 during low-Re operations, the magnitude of the drop in e_0 increases with decreasing Re.

Lift-curve slope results show a decreasing trend with increasing $Æ$ (Fig. 13(c)). Additionally, on comparing the results with analytical predictions from lifting-line theory and Hembold equation, we observe that, barring the lift-curve slope of the Vapor, analytical methods overpredict C_{L_α} for wings operating at low Reynolds numbers. To understand the reason as to why the analytical methods predict the C_{L_α} with reasonable accuracy, despite the Vapor being affected by low-Re effects, we refer to the experiments conducted by Torres et al. [28] on flat plates with aspect ratios below 3. They observed a lift curve slope of 0.056 per degree at $Æ$ for an elliptically loaded wing, which matches with the current data for the Vapor sUAV which has an elliptical flat wing with an aspect ratio of 2.56 and exhibits a lift curve slope of 0.0574 per degree. Furthermore, Torres et al. [28] concluded that, within the range of aspect ratios they tested, efficiency factors ranging from 0.5 to 0.8 were consistent with the expressions derived from lifting line theory for an elliptically loaded wing, thereby confirming the results observed in Fig. 13(a) for the Vapor. Similarly, in a study conducted by Okamoto and Azuma [35], elliptical wings with aspect ratios ranging from 1 to 8 were investigated. Their study reported a lift curve slope of 0.043 per degree for a wing with an aspect ratio of $Æ$. For the other five sUAVs, which had non-elliptical wings, the deviation in C_{L_α} from analytical predictions were in line with observations made by Spedding and McArthur [23], who attributed the limitations of the analytical predictions to their inability to account for low-Re effects. While Spedding and McArthur [23] introduced a correction factor to the theory, a high-level of uncertainty in the applicability of said correction was acknowledged.

5.3 Stability analysis

Understanding the factors that affect the stability of sUAVs holds immense value in their design and operation [3]. Stability refers to the ability of an sUAV to maintain a balanced and controlled flight, resisting deviations from its intended trajectory, and effectively countering external disturbances. The current analysis focuses on evaluating the longitudinal stability, lateral stability and phugoid mode characteristics of the sUAVs and the attendant ability of the motion capture system to provide insights into their inherent stability, dynamic response and oscillatory behaviour. While all six sUAVs are considered for the phugoid mode analysis, only the TR-C285G and F4U-Corsair aircraft are used for the lateral and longitudinal stability analysis due to the availability of their respective wing cross-sectional geometry and attendant aerodynamic forces and moments (using XFOIL).

5.3.1 Longitudinal stability

Longitudinal stability pertains to the capability of an aircraft to retain control over its pitch axis and regain its original trim angle-of-attack when subjected to disturbances. To achieve longitudinal stability, several factors come into play including the positioning and design of the aircraft's wings, horizontal

stabiliser and elevator. The wing generates lift while the horizontal stabiliser and elevator work together to create forces that counteract any deviations in pitch and restore stability. Additionally, longitudinal stability is intricately tied to the neutral point, which is fundamentally associated with the aircraft's CG. The neutral point denotes a specific position on the aircraft's longitudinal axis where alterations in lift forces exert minimal influence on the pitching moment experienced by the aircraft. When the CG is positioned ahead of the neutral point the aircraft typically exhibits longitudinal stability. In such a config-uration, if the aircraft encounters a nose-up disturbance the increased lift generated by the wings creates a pitching moment that counteracts the disturbance, assisting the aircraft in returning to its original trim angle. Conversely, when the CG is located aft of the neutral point, the aircraft tends to be longitudinally unstable. In this scenario, a nose-up disturbance prompts the aircraft to generate a pitching moment that magnifies the disturbance, resulting in a greater deviation from the trim angle. When a precise angle, δ_e, is applied to the elevator deflection, it causes the aircraft to experience a shift in its pitch attitude, resulting in a noticeable pitch-up or pitch-down motion. This alteration in elevator deflection influences the distribution of lift across the wings, which in turn affects the overall pitching moment coefficient (C_{M_α}) generated by the aircraft. Consequently, these changes in the pitching moment coefficient impact the position of the neutral point.

The aircraft's trim angle-of-attack can be determined through the analysis of the slope C_{M_α}, where α_{trim} is the angle-of-attack corresponding to $C_M = 0$ for each individual elevator deflection angle. The neutral point is then calculated by,

$$X_{np} = \frac{C_{L_{\alpha,w}} \bar{x}_{ac,w} + C_{L_{\alpha,h}} \bar{x}_{ac,h} \eta_h \frac{S_h}{S_{ref}} \left(1 - \frac{\partial \varepsilon}{\partial \alpha}\right)}{C_{L_{\alpha,w}} + C_{L_{\alpha,h}} \eta_h \frac{S_h}{S_{ref}} \left(1 - \frac{\partial \varepsilon}{\partial \alpha}\right)} \tag{18}$$

where the subscripts w and h represent wing and horizontal tail respectively. $\bar{x}_{ac}$ is the aerodynamic centre, and was assumed to be at 25% chord. S_{ref}, and S_h represent the reference areas of the wing and horizontal tail. The downwash from the main wing $\frac{\partial \varepsilon}{\partial \alpha}$ was assumed to be 0.45, and the velocity deficit ratio η_h was set to be 0.8 from theoretical calculations [3]. Figure 14 shows the neutral point (X_{np}) with respect of trim angle-of-attack (α_{trim}) and is compared to the CG location of both sUAVs. The measurements are made from the wing root leading edge and are non-dimensionalised with respect to the wing root chord. The results obtained for both aircraft indicate that the neutral point is in close proximity to the CG, thereby indicating that both sUAVs are longitudinally stable at the conditions tested (small-to-moderate elevator deflection inputs, typically ranging between -10 to 10 degrees). However, the TR-C285G displayed a rearward shift of its neutral point in relation to the CG at negative as well as angles of attack higher than 8 degrees, indicating an aftward shift of the neutral point with respect to the CG, and therefore imminent longitudinal instability.

5.3.2 Lateral stability

Lateral stability in the context of sUAVs pertains to the aircraft's capacity to sustain stable flight in the lateral axis direction. It encompasses the inherent ability of the sUAV to counteract rolling movements and uphold a level attitude throughout the flight. In the current work, we focus on examining the exper-imental weather vane stability (C_{n_β}) and roll stability (C_{l_β}). Weather vane stability measures the yawing response of an aircraft caused by a sideslip angle and is measured using the equation,

$$C_{n_\beta} = \eta_v \forall_v a_v \left(1 + \frac{d\sigma}{d\beta}\right) - 2\frac{\forall}{Sb} \tag{19}$$

where η_v is the vertical tail efficiency factor, a_v is vertical tail angle-of-attack, $\forall_v$ is the tail volume ratio, and $\forall$ is the volume of the equivalent fuselage. A positive weather vane stability coefficient indicates the aircraft's inclination to align itself with the relative wind while a negative value suggests a propensity for the aircraft to deviate from its intended heading. Figure 15(a) plots the weather vane stability for the two sUAVs as a function of trim angle-of-attack. We observe that, at all trim angles, the TR-C285G consistently exhibited positive weather vane stability. In contrast, the F4U-Corsair displayed instability
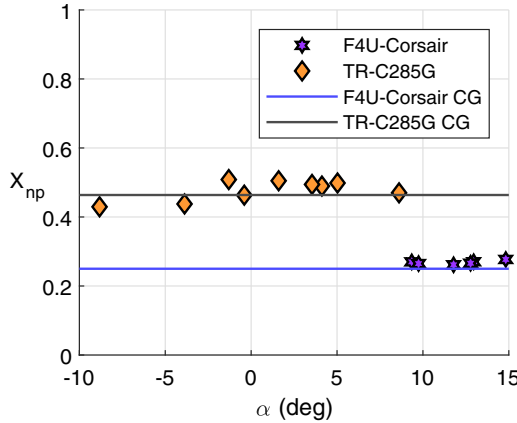
Figure 14. *Experimental neutral point and CG versus trim angle-of-attack.*

beyond an angle-of-attack of 15 degrees, at which point any sideslip was not being dampened out. Additionally, at an approximate trim angle-of-attack of ~ 10 degrees, a slight negative value of C_{n_β} was observed, indicating marginal instability of the aircraft.

Roll stability (dihedral effect) is equated using the equation,

$$C_{l_\beta} = -\frac{2}{3\pi} a_w \sin(\Gamma) \qquad (20)$$

where a_w is the wing angle-of-attack and Γ is the geometric angle of dihedral. Given that C_{l_β} is a function of dihedral, roll stability was only analysed for the F4U-Corsair aircraft as the TR-C285G does not have any dihedral. Negative values of roll stability indicate stable conditions where the aircraft has the ability to attenuate and stabilise against any disturbances or perturbations. Results for the F4U-Corsair, plotted in Fig. 15(b), show a negative C_{l_β} at all trim angles of attack, indicating roll stability across the tested flight conditions.

5.3.3 Dynamic stability

Dynamic stability of an aircraft can be determined by analysing its phugoid mode, characterised by a unique longitudinal oscillation pattern featuring extended durations of climbing and descending flight paths. During the phugoid mode, the aircraft continuously exchanges energy between potential and kinetic forms as it cyclically trades altitude for airspeed. The dynamic interplay between altitude and velocity helps maintain the stability and equilibrium of the aircraft during flight. By carefully monitoring the flight's time history and analysing the variations in altitude, the phugoid half period can be identified. The method of extracting the phugoid half period is illustrated in Fig. 16(a) using data for a single flight of the TR-C285G aircraft. By co-plotting the time history of the altitude changes and corresponding airspeed, we observe that the TR-C285G demonstrates a half period of approximately 1 second for the given flight. Similar behaviour was observed across multiple flight instances of the aircraft as well. The process was repeated for multiple flight data sets for all six sUAVs to determine their respective phugoid periods. To verify the results, the measured phugoid period was compared with theoretical predictions. The natural frequency of the phugoid is mainly a function of gravitational acceleration (g) and velocity (V) when neglecting compressibility effects [36, 37]. The linear longitudinal equation of motion can therefore be approximated to $\sqrt{2}\frac{g}{V}$ to evaluate the theoretical natural phugoid frequency ($\omega_{n,ph}$) and hence the phugoid period. Figure 16(b) shows the comparison between the theoretical phugoid period and the experimentally observed period. The sUAVs that were flown within specific speed regimes exhibited good agreement with theoretical predictions thereby confirming the capability
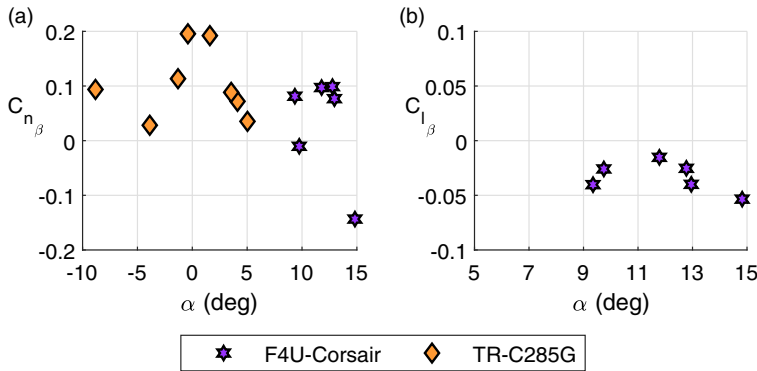
Figure 15. *Experimental (a) weather vane stability and (b) roll stability.*
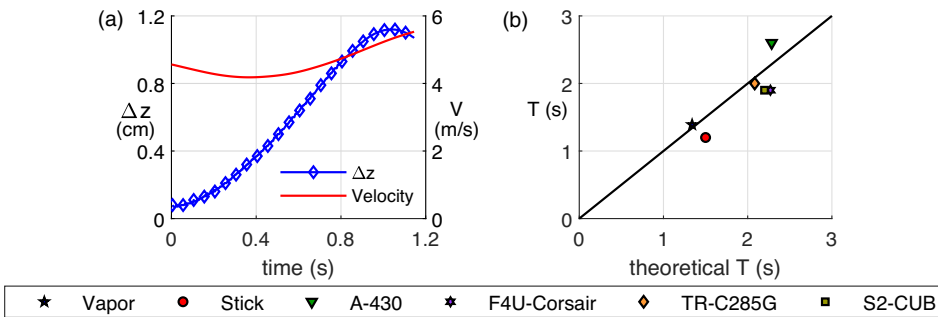

Figure 16. *Phugoid mode analysis: (a) time history of altitude and airspeed and (b) comparison between the experimental and theoretical phugoid period.*

of the motion capture system in effectively capturing the essential dynamics of the phugoid modes for sUAVs.

6.0 Conclusion

The objective of this study was to utilise an existing motion capture system to aerodynamically characterise sUAVs via off-board measurements and study the effects of low-Re conditions on the aircraft aerodynamics. Initial efforts were centred around assessing system uncertainties through static tests to examine the standard deviation in position and attitude for a stationary aircraft and dynamic tests to ascertain the system's accuracy in determining body acceleration by measuring the acceleration due to gravity during free fall. Subsequently, flight data for six sUAVs were successfully acquired, with the analysis primarily focused on quasi-steady flight conditions. To gain insights into the influence of low Reynolds number effects on the aerodynamic data, trends in the Oswald efficiency factor and lift curve-slope were investigated. Lastly, a comprehensive stability analysis was carried out to ascertain the effectiveness of the motion capture system in characterising flight stability.

Uncertainty analysis of the motion capture system showed that the standard deviation in position and attitude measurements were less than 0.05mm and 0.02 degrees, respectively. Additionally, the free-fall tests demonstrated that the error in acceleration measured by the motion capture system was less than 0.025%. Analysis of the aerodynamic data measured for the six sUAVs with aspect ratios ranging from 2 to 6.3 revealed trends in Oswald efficiency factors and lift-curve slope that clearly showed the effect of low Reynolds number on the flight aerodynamics. While low aspect ratio wings ($\mathcal{R} < 4$) had Oswald

efficiency factors above 0.65 and matched with theoretical predictions, increasing the aspect ratio led to a sharp drop in Oswald efficiency factors (< 0.4). The above trends matched with low Reynolds number wing data from literature, with the sharp drop in e_0 being attributed to low Reynolds number effects. Lift curve slope measurements matched well with theory for aircraft with elliptical wings but were observed to be lower than theoretical predictions for non-elliptical wings, as expected. Additionally, the lift-curve slope was observed to decrease with increasing wing aspect ratio. Stability analysis of the captured flight data for the F4U-Corsair and the TR-C285G aircraft showed that the neutral point tended to cluster around the centre of gravity location across the range of trim angles tested, showing lateral stability. Both aircraft also showed positive weather vane stability across all trim angles. Additionally, the F4U-Corsair displayed roll stability across all trim angles tested. Dynamic stability analysis, determined by the phugoid mode, showed the measured phugoid period matching well with theoretical predictions.

Overall, in addition to successfully demonstrating the capability of the motion capture method in characterising the aerodynamic and stability characteristics of sUAVs (via experimental and analytical validation), the current research adds new knowledge to existing literature by shedding light on the effects of low-*Re* flows on the Oswald efficiency factors and lift-curve slopes for sUAVs with varying wing aspect ratios.

References

[1] Pines, J.D. and Bohorquez, F. Challenges facing future micro-air-vehicle development, *J. Aircraft*, 2006, **43**, pp 290–305.

[2] Mueller, J.T. On the birth of micro air vehicles, *Int. J. Micro Air Veh.*, 2009, **1**, (1), pp 1–12.

[3] Uhlig, V.D. Micro Air Vehicle Motion Tracking and Aerodynamic Modeling. PhD dissertation, University of Illinois, 2014.

[4] Mettler, F.B. Extracting micro air vehicles aerodynamic forces and coefficients in free flight using visual motion tracking techniques, *Exp. Fluids*, 2010, **49**, pp 557–569.

[5] Krashanitsa, Y.R., Silin, D., Shkarayev, S.V. and Abate, G. Flight dynamics of a flapping-wing air vehicle, *Int. J. Micro Air Veh.*, 2009, **1**, (1), pp 35–49.

[6] Mueller, J.T. Aerodynamic measurements at low reynolds numbers for fixed wing micro-air vehicles, *RTO AVT/VKI Spec. Course*, 1999, **8**, pp 1–32.

[7] Pelletier, A. and Mueller, T.J. Low reynolds number aerodynamics of low-aspect-ratio, thin/flat/cambered-plate wings, *J. Aircraft*, 2000, **37**, pp 825–832.

[8] Ifju, P., Waszak, M. and Jenkins, L. Stability and control properties of an aeroelastic fixed wing micro aerial vehicle, AIAA paper 2001-4005, 2001.

[9] Johnson, N.E., Turbe, A.M., Wu, D.A., Kannan, K.S. and Neidhoefer, C.J. Flight test results of autonomous fixed-wing uav transitions to and from stationary hover, AIAA paper 2006-6775, 2006.

[10] Rhinehart, M. and Mettler, B. Extracting aerodynamic coefficients using direct trajectory sampling, AIAA paper 2008-6899, 2008.

[11] Uhlig, V.D. and Selig, S.M. Stability characteristics of micro air vehicles from experimental measurements, AIAA paper 2011-3659, 2011.

[12] Rao, H.A., Uhlig, V.D. and Selig, S.M. Glide and powered flight characteristics of micro air vehicles from experimental measurements, AIAA paper 2012-2768, 2012.

[13] Selig, M. Modeling full-envelope aerodynamics of small uavs in realtime, AIAA paper 2010-7635, 2010.

[14] Uhlig, V.D. and Selig, S.M. Modeling micro air vehicle aerodynamics in unsteady high angle-of-attack flight, *J. Aircraft*, 2017, **54**, pp 1064–1075.

[15] Woollands, M.R. System identification modeling of micro air vehicles from visual motion tracking data, Master's thesis, University of Minnesota, 2010.

[16] Uhlig, V.D. and Selig, S.M. Determining aerodynamic characteristics of a micro air vehicle using motion tracking, *J. Aircraft*, 2013, **50**, (5), pp 1481–1490.

[17] Cory, R. and Tedrake, R. Experiments in fixed-wing uav perching, AIAA paper 2008-7256, 2008.

[18] Cory, E.R. Supermaneuverable Perching, PhD thesis, Massachusetts Institute of Technology, 2010.

[19] Uhlig, V.D., Sareen, A., Sukumar, P., Rao, A.H. and Selig, M.S. Determining aerodynamic characteristics of a micro air vehicle using motion tracking, AIAA paper 2010-8416, 2010.

[20] Paranjape, A.A., Kim, J., Gandhi, N. and Jo Chung, S. Experimental demonstration of perching by an articulated wing mav, AIAA paper 2011-6403, 2011.

[21] Moore, L.J. Robust Post-Stall Perching with a Fixed-Wing UAV, PhD thesis, Massachusetts Institute of Technology, 2014.
[22] Selig, S. and Mcgranahan, D.B.M. Airfoils at low speeds. Technical Report Soartech 8, 1989.
[23] Spedding, R.G. and McArthur, J. Span efficiencies of wings at low Reynolds numbers, *J. Aircraft*, 2010, **47**, pp 120–128.
[24] Laitone, V.E. Wind tunnel tests of wings at reynolds numbers below 70 000, *Exp. Fluids*, 1997, **23**, (5), pp 405–409.
[25] Selig, S. and Mcgranahan, D.B.M. Wind tunnel aerodynamic tests of six airfoils for use on small wind turbines, Technical Report NREL-500-34515, 2004.
[26] Lyon, A.C., Broeren, P.A., Giguere, P., Gopalarathnam, A. and Selig, M.S. *Summary of Low Speed Airfoil Data: Volume 3*, SoarTech Publications, 1997.
[27] Ananda, K.G., Sukumar, P.P. and Selig, S.M. Measured aerodynamic characteristics of wings at low Reynolds numbers, *Aerospace Sci. Technol.*, 2015, **42**, pp 392–406.
[28] Torres, G. and Mueller, T. Low-aspect-raito wing aerodynamics at low reynolds numbers, *AIAA J.*, 2004, **42**, pp 865–873.
[29] Ananda, K.G., Sukumar, P.P. and Selig, S.M. Low-to-moderate aspect ratio wings tested at low Reynolds numbers, AIAA Paper 2012–3026, 2012.
[30] Optitrack. Optitrack: Motion capture system, 2022.
[31] Wolowicz, H.C. and Yancey, B.R. Experimental Determination of Airplane Mass and Inertial Characteristics, NASA TR R-433, October 1974.
[32] SensorsONE. Local gravity calculator, 2022.
[33] Barford, G.N. *Experimental Measurements: Precision, Error, and Truth*, 2nd ed, John Wiley & Sons, 1998, New York, NY.
[34] Cooper, E.J. and Wright, R.J. *Introduction to Aircraft Aeroelasticity and Loads*, 2nd ed, John Wiley Sons, Ltd., 2014.
[35] Okamoto, M. and Azuma, A. Aerodynamic characteristics at low Reynolds numbers for wings of various planforms, *AIAA J.*, 2011, **49**(6), pp 1135–1150.
[36] Nelson, C.R. *Flight Stability and Automatic Control*, 2nd ed, WCB/McGraw Hill, 1998, New York.
[37] Bossert, E.D., Hallgren, F.W., Yechout, R.T. and Morris, L.S. *Introduction to Aircraft Flight Mechanics: Performance, Static Stability, Dynamic Stability, and Classical Feedback Control*, 2nd ed, AIAA Education Series. AIAA, 1998.

Appendix

A. Appendix

Flight data for the Micro Stick Vintage, Edge A-340, and S2-CUB sUAVs have been provided in the current section.
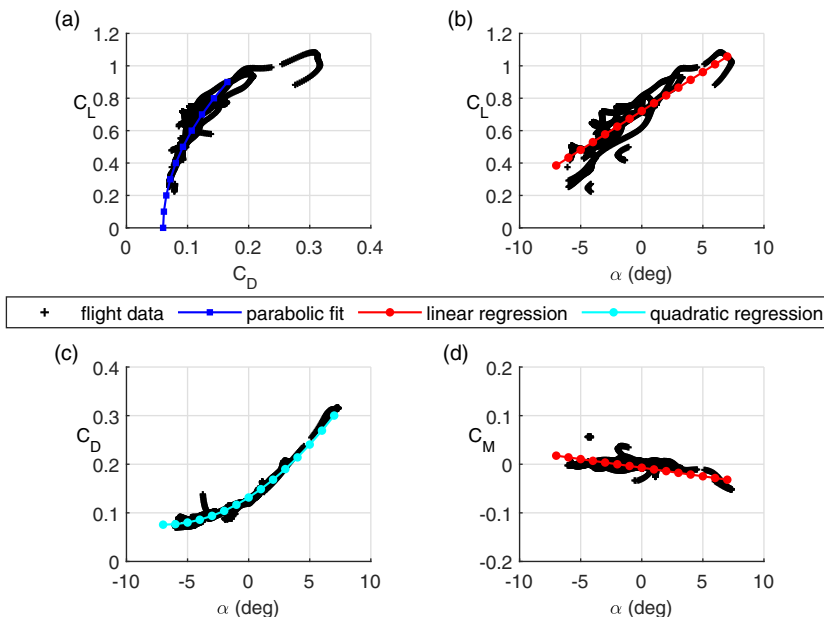

Figure A1. *Flight data for the Micro Stick Vintage ($\mathcal{R} = 3.8$): (a) experimental drag polar with parabolic fit, (b) experimental lift curve with linear regression, (c) experimental drag curve with quadratic regression and (d) experimental pitching moment with linear regression.*
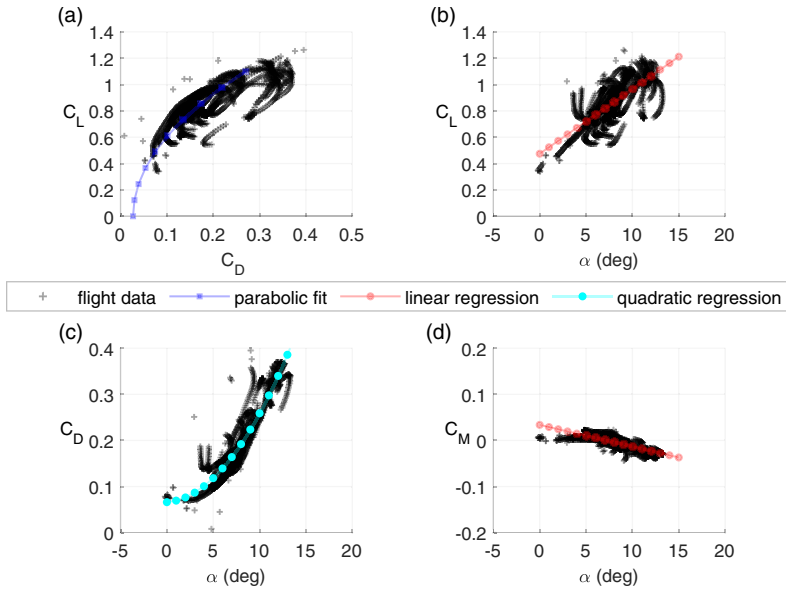
Figure A2. *Flight data for the Edge A-430 ($\mathcal{R} = 4.5$): (a) experimental drag polar with parabolic fit, (b) experimental lift curve with linear regression, (c) experimental drag curve with quadratic regression and (d) experimental pitching moment with linear regression.*
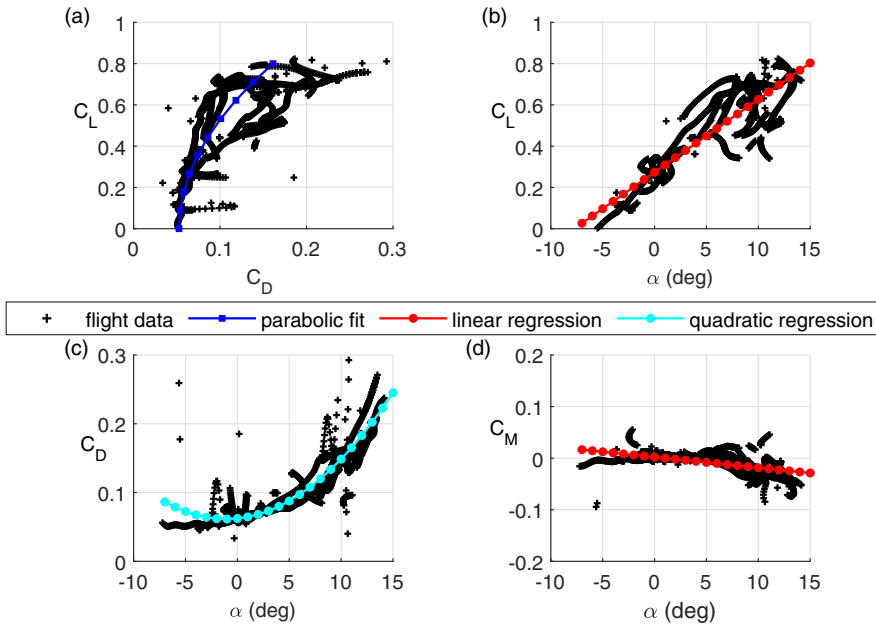

Figure A3. *Flight data for the S2-CUB ($\mathcal{R} = 6.32$): (a) experimental drag polar with parabolic fit, (b) experimental lift curve with linear regression, (c) experimental drag curve with quadratic regression and (d) experimental pitching moment with linear regression.*